Towards a Method of Estimating Out-of-Plane Effects on Measurements of Turbulent Flame Dynamics

Ankit Tyagi and Jacqueline O'Connor
Mechanical Engineering, Pennsylvania State University, University Park, PA, 16802

Corresponding author
Jacqueline O'Connor
111 Research East Building
University Park, PA 16802
814.863.1502, jxo22@psu.edu

Abstract

   Turbulent flames are highly three-dimensional and while planar measurement techniques for studying these flames are widely used, the interpretation of two-dimensional flame data can suffer from three-dimensional, out-of-plane effects. In this study, a methodology to statistically estimate three-dimensional effects on flame propagation measured from planar high-speed measurements is presented. This methodology uses a theoretical approach to estimate the out-of-plane motion effects on flame propagation and probabilistic modeling to separate this effect from measured experimental data. The methodology is applied to the consumption speeds of reactant pockets in a rectangular Bunsen flame experiment in this study. Simultaneous s-PIV and OH-PLIF measurements are performed to track the behavior of reactant pockets and obtain their consumption rates. A univariate mixture model is used to model the experimental data and a distribution reflecting the out-of-plane motion contribution of the consumption speed is obtained by modeling three-dimensional pockets and convecting them through a plane based on the measured pocket edges and out-of-plane velocities. A Markov-chain Monte Carlo approach is used to separate the two distributions and uncertainties are estimated in the experimental consumption speed data. Finally, we discuss the applicability of this approach to experimental measurements.

Keywords: Turbulent flame, planar laser diagnostics, uncertainty estimation

Nomenclature

Acronyms

2D	Two-dimensional
3D	Three-dimensional
DNS	Direct numerical simulation
FOV	Field of view
MCMC	Markov-chain Monte Carlo
MS	Mie-scattering
PDF	Probability density function
PLIF	Planar laser-induced fluorescence
s-PIV	Stereoscopic-particle image velocimetry

Symbols

A	Pocket surface area
C_T	Image thresholding cutoff
I_{xx}	Moment of inertia about the x-axis
I_{yy}	Moment of inertia about the y-axis
P	Pocket perimeter
S_a	Surface area
S_C	Pocket consumption speed
$S_{C,3D}$	Three-dimensional pocket consumption speed
U	Mean flow velocity
$\bar{U}_z$	Mean out-of-plane velocity within a pocket
V	Volume
b	Variance parameter in Cauchy distribution
$\bar{c}$	Time-averaged progress variable
n	Order of Legendre polynomial
r	Pocket radius
s_L	Laminar flame speed
t	Time
u'	Turbulence intensity
x	Streamwise direction
y	Cross-stream direction
z	Spanwise direction
λ	Variance parameter in Inverse Gaussian distribution
μ	Mean variable in the Cauchy and Inverse Gaussian distributions
$\hat{\pi}$	Mixing parameter
σ	Fit variance

1   Introduction

The use of planar laser diagnostics for measurement of premixed turbulent flames is ubiquitous. The increased availability of high-speed planar laser-induced fluorescence (PLIF) systems for identifying species such as OH, CH, CH_2O, and others has allowed a large number of researchers to investigate the structure and dynamics of flames. In particular, the use of OH- and CH-PLIF for tracking flame edges has been used in a wide variety of premixed flame studies, including turbulent Bunsen flames [1-3], bluff-body flames [4-6], and swirl-stabilized flames [7-9]. Though these studies have significantly enhanced our understanding of turbulent flame dynamics, there is still uncertainty as to the impact of out-of-plane behavior on the interpretation of results measured in plane [10]. The use of multiple laser planes [5, 11], laser plane sweeps [12, 13], or simultaneous imaging techniques [14] improve upon single-sheet imaging but are often prohibitively complex or equipment-intensive to use consistently. The goal of this work is to propose a framework by which theory and probabilistic modeling can be used to estimate the contribution from out-of-plane effects. We limit ourselves, initially, to measurement of turbulent flame dynamics, rather than measurement of chemical kinetics.

One obvious counterpoint to this goal is the use of volumetric flame imaging techniques. These techniques generally fall into two categories: light field techniques and tomographic techniques. Light field techniques [15] require the use of plenoptic cameras, where an array of microlenses is used to image a volume at various focal lengths, or structured illumination [16], where a number of "coded" laser planes at different locations are imaged and the image is decomposed using the shape that is coded into the laser plane. The reconstruction of these light-field images is computationally intensive and, as noted by Greene and Sick [17], the loss of resolution and low signal to noise ratio make these techniques difficult for flame imaging. Volumetric laser-induced fluorescence (VLIF) is another option that has been explored by volumetrically illuminating a region of the flame and imaging the region with multiple cameras, sometimes operated with multiple views. A number of different volumetric measurements have been made, including CH-LIF [18], OH-LIF [19, 20], CH_2O- and PAH-LIF [21], and iodine-LIF [22]. The benefits of such a technique are clear – the instantaneous, three-dimensional (3D) imaging of flame surfaces provides information about flame structure and dynamics. The drawbacks, however, are also significant. Loss of spatial resolution has been noted in comparison to two-dimensional (2D) PLIF [18, 23]; for example, Ma *et al.* [23] quoted a difference in PLIF and VLIF resolution with a pixel

size of 0.041 mm in PLIF and a voxel size of 0.18 mm in VLIF. Further, there are significant hardware requirements for this technique. Assuming that these intensive resources are not available to every researcher, methods for more accurate interpretation of planar images are necessary.

There are several out-of-plane effects that can arise in the measurement of turbulent flame dynamics. As turbulent flames are inherently three-dimensional, measurement of the flame surface in a plane will not capture its rich topology. One of the first issues is robustly identifying a flame normal. Work by Coriton and coworkers [24-26] showed the issues related to flame normal definition in a volumetric particle image velocimetry (PIV) study of the principle strain rates in the vicinity of flames. The flame edge was defined using PLIF and the assumption was made that the flame was nominally oriented perpendicular to the volume of the PIV measurement as a result of the flame configuration. However, at high enough turbulence intensities, this assumption breaks down and defining a flame normal is difficult with a planar measurement. Previous researchers have also used multiple-plane techniques or data filtering to avoid this issue. Work by Trunk *et al.* [27] used a dual-plane OH-PLIF measurement simultaneously with stereoscopic PIV (s-PIV) to identify the flame-normal orientation in order to calculate local flame speed. A NURBS spline fitting algorithm [28] was used to estimate the 3D flame surface between the planes and the flame surface normal was calculated in the center where the s-PIV measurement was made, allowing for calculation of the displacement speed. The same technique was used by Peterson *et al.* [29] in a spark-ignition engine. The identification of a flame normal is particularly important in the study of edge flames. Work by Grib [30] considered the effect of curvature on the propagation speed of edge flames in stratified media using simultaneous PIV and OH-PLIF measurements. In order to ensure that the measured flow velocity ahead of the edge flame was truly the propagation speed of the edge, the authors only kept data points where the flames were uniform in the out-of-plane direction.

A similar issue arises with the definition of flame curvature, which requires the calculation of gradients in three-dimensional space [31]. Direct numerical simulation (DNS) has highlighted the three-dimensionality of flame surfaces and the importance of flame curvature on flame propagation. DNS from Bell *et al.* [31] in a planar Bunsen flame highlighted the 3D nature of the flame shape. Analysis of these detailed calculations, like those done by Dasgupta *et al*. [32], have

4

allowed for highly-detailed descriptions of the flame chemistry and its changes in the presence of turbulence; these showed that chemical pathways can change in regions of high curvature due to the effect of flame strain [33]. Three-dimensional flame curvature measurements were made by Ma *et al.* [34] using tomographic chemiluminescence imaging. Six high-speed cameras were used to simultaneously image a planar Bunsen flame and an algebraic reconstruction technique [35] was used to calculate the shape and local 3D curvatures.

The measurement of displacement speed also suffers in a planar measurement as the normal to the flame cannot be rigorously defined. Previous work has tried to circumvent this issue by either measuring in multiple planes, as discussed before, or calculating flame displacement speeds in flame geometries where displacement can be measured at a point rather than a surface. For example, work by Marshall *et al.* [36, 37] used a low-swirl burner [38] to measure turbulent displacement speeds and local flame curvatures in syngas flames. They chose this configuration as the leading point of the flame is nominally one-dimensional [39], which reduces uncertainty of planar measurements. However, images of the flame edges at turbulent conditions show highly wrinkled flames that likely violate this quasi-1D assumption.

The measurement of consumption speed is affected by planar measurements as the area of the flame measured in the laser plane may not be representative of the total surface area of the flame, making a calculation of mass flow rate through the surface difficult. Zhang *et al.* [40] overcame this difficulty in measuring global consumption speed in a circular Bunsen flame using 2D LIF imaging and a number of assumptions about the structure of the flame. They assumed that the jet flow was statistically 2D, that the OH-PLIF measurement plane was symmetric about the centerline of the Bunsen burner, and that flame motion out of plane had similar statistics to the motion in the plane. Using these assumptions, they implemented five theoretical models that related 3D and 2D flame surface density to estimate the 3D flame behavior from their planar images. While the differences in the models could be as high as 50%, they provided important insight into the structure of turbulent flames. Their follow-on work [41] further clarified differences between 2D and 3D flame topologies using CH-PLIF and tomographic chemiluminescence imaging.

Data from our planar turbulent Bunsen flame is in Figure 1, which shows PDFs of the consumption speed of flame pockets [42]. In this work, we identified pockets of reactants that

separated from the main flame surface using a non-rigid image registration technique, described in detail in Tyagi *et al.* [43]. These pockets were tracked through space and their consumption rate calculated by knowing the pocket area and perimeter in the plane of the laser: $S_C = \Delta A/P_1\Delta t$. In a 3D sense, consumption speed can be calculated by $S_{C,3D} = \Delta V/S_a\Delta t$, which requires knowledge of both the volume and surface area of the flame at any given time. The 2D formulation approximates the 3D form, but can be biased by the region of the pocket that is captured in the plane of the laser.

Even in a statistical sense, the consumption speed calculations have an issue, which is evidenced in the PDFs in Figure 1. These PDFs show that some percentage of the pockets have a negative consumption speed, which is not physical for reactant pocket consumption at the turbulence intensities present in this experiment (u'/s_L=5.5 – 12.6). We believe that the negative consumption speeds are an artifact of making a planar measurement of a three-dimensional object. As such, the measured consumption rates are actually a combination of actual consumption speeds and apparent consumption speeds due to the planar measurement.

It is this previous work on tracking the behavior of flame pockets in turbulent Bunsen flames [42] that led us to investigate ways to estimate how planar measurements affect the measurement of consumption speed PDFs. The remainder of this paper outlines a new method for estimating the extent to which pocket consumption rate measurements are affected by planar diagnostics. First, we describe the biases present in planar measurements of consumption speeds through analysis of a pocket generated in DNS. Next, we describe the experimental setup and data collection technique by which we obtained turbulent flame pocket data. Third, we discuss the formulation of our out-of-plane estimation technique, which uses probabilistic modeling and Markov-chain Monte-Carlo (MCMC) methods to estimate the impact of out-of-plane behavior on the consumption speed distribution. Then, we present and discuss the results of this method on a representative data set from our previous work [42]. Finally, we discuss pathways for extension of this work.

2   Planar Measurements of Flame Pockets

To understand the potential errors that arise from planar measurements of pocket consumption speed, we analyze a pocket burn-out event from a DNS provided by Dr. Peter Hamlington at CU-Boulder [44]. The simulation encompasses 2.49×10^{-3} seconds of a premixed, stoichiometric methane-air flame at an unburnt mixture temperature of 300 K and a Karlovitz number of 100. The

simulation domain is 256x256x4096 cells with a spatial resolution of 2.73×10^{-5} m and a time stepping of CFL=0.3. The simulation resolves about 0.5 Kolmogorov scales per grid cell in the reactants and 6 in the products. The simulation was initially run for a duration of 2.28×10^{-3} seconds with sparse data collection in time until a pocket structure was found in the time series; the simulation was then re-run around that pocket time with a temporal sampling of 8.6×10^{-9} s. Altogether, the simulation took about 167 hours and 1,378,944 CPU hours to calculate on a 125,440 core U.S. Department of Defense supercomputer, Topaz.

Figure 2 shows the pocket burn-out event in time. The pocket was originally formed through a cusping event (not shown), causing the pocket to break away from the main flame surface. The pocket is initially irregularly shaped; certain parts of the pocket are convex and others concave and the aspect ratio of the pocket is high. As the pocket burns out, it pinches off, resulting in a second smaller pocket that is not tracked in this calculation. After approximately 0.15 ms, the pocket completely burns out.

Figure 3 (a) shows the time series of the 3D consumption rate calculation at each time step. The consumption rate spikes where the pocket splits in two as a result of the significant loss of volume. The consumption rate accelerates as the pocket burns out, likely a result of both the smaller volume to area ratio as well as the speed-enhancing effect of high curvature. Figure 3(b) shows a histogram and PDF of the speeds over the burn-out event. In this calculation, all speeds are positive as the pocket continually decreases in volume throughout its lifetime. Further, the distribution is skewed towards higher speeds as a result of the consumption speed acceleration at the end of burn-out.

To understand the results we would obtain with a planar measurement, we observe the pocket in a number of planes. Figure 4(a,b) show the initial shape of the DNS pocket and three planes in the Cartesian coordinate system of the simulation centered at the centroid of the pocket. Given the high aspect ratio of the pocket, the shape that appears in the yz plane is significantly different than those in the xy and xz planes. To compare 2D pocket consumption rates in different planes, we vary the plane orientation and location in two ways. First, we peg the origin of the planes to the initial centroid of the pocket and rotate the planes yz and xz about the z-axis from 0 to 90 degrees, measuring the 2D consumption rate of the pocket in time at each of the rotation angles. Additionally, we move the planes in a direction perpendicular to their original orientation with

distances as large as 1.88 mm in either direction, away from the centroid, and then measure the 2D consumption rates at the same range of rotation angles. To quantify the consumption of reactant gases inside tracked pockets, a pocket global consumption rate is formulated as:

$$S_C = \Delta A / P_1 \Delta t \tag{1}$$

In Equation (1), ΔA is the area consumption due to reactant gas consumption in the plane of measurement for a time interval of Δt and P_1 is the perimeter of the pocket at any time t_0. Figure 5(a) shows a histogram of the 2D measurements in planes yz and xz for all angles and displacements, along with the true 3D consumption rates; note the existence of negative consumption rates in these histograms. The differences in the histograms between planes indicate that the orientation and shape of the pocket can result in an erroneous measurement of the pocket consumption rate. Figure 5(b) shows six different examples of 2D consumption rate time series that include negative consumption rates. In general, the 2D consumption rate trends follows that of the 3D consumption rate, although many have features that diverge from the 3D trend. Examples 1 and 4 show the consumption rates calculated in the non-rotated xz and yz planes at the centroid of the pocket. The consumption time series for plane xz shows a peak similar to the 3D time series at the moment of pocket splitting and a sharp increase near t=1.22 ms as the pocket burns out in-plane. The same time series for plane yz does not exhibit any peak when the pocket splits. Examples 2 and 5, with planes xz and yz located away from the initial pocket centroid, have consumption rates that are biased towards negative values. In particular, the xz plane calculations suffer from the non-convex, high aspect ratio shape, whereas the yz plane calculations are influenced by the flame surface pinch-off from pocket splitting and the non-convex shape of the flame surface. Finally, in Examples 3 and 6, the influence of the out-of-plane motion of the pocket can be observed; for both planes xz and $yz,$ it can be seen that a slight offset of the plane location from the initial centroid greatly enhances the pocket motion effect. Both time series show instances where increases in 2D flame areas due to the pocket motion through these planes exist, resulting in a negative bias in the consumption rates.

These time series show the variety of physical processes that can influence a 2D measurement of a 3D object, particularly in cases with both flow convection and surface propagation. It is unclear whether even the aggregate of thousands of 2D measurements of thousands of different

8

pockets would replicate the 3D trend due to the complexities of pocket shapes and the imbalance between convection and propagation. Future work should include a deeper analysis of DNS data or pockets modeled using other methods like level-set approaches [45], as the conclusions from the analysis of many different views of one single pocket do not capture the independent statistics that would be required to show with high statistical significance the relationships between 2D and 3D pocket behaviors. However, we do believe that we can estimate the biases introduced by a planar measurement using theory and understand the impact of these biases on the consumption rate distributions using mixed-model methods. The remainder of this paper describes a method to do this process. We choose out-of-plane motion as the bias to correct as we know that there are out-of-plane flow biases in the experiment; as such, we expected that the out-of-plane motion component to be significant. This methodology could be applied to any of these biases, as will be discussed in more detail in Section 6.

3 Experimental Configuration

3.1 Experiment

A multi-plane experiment was performed to measure pocket formation and burn-out in a turbulent Bunsen flame. The burner is the same that was used by Tyagi *et al.* [43] and so a brief overview of the experiment is provided here. The burner consists of a 100 mm x 10 mm exit plane and contains two layers of ceramic honeycombs for flow conditioning and a set of perforated plates for turbulence generation. The turbulence plates are located 30 mm and 10 mm upstream of the burner exit and result in generation of averaged non-reacting flow turbulence intensities of 18% at the burner exit. Two types of pilot flames are used: small "anchoring" pilots for anchoring the main flame to the burner walls and "back-support" pilots for providing adiabatic combustion products around the flame. The pilot and main flames burn mixtures of natural gas and air at an equivalence ratio of 1.0. The bulk flow velocity of the main burner is 12 m/s (11.97 g/s), and the bulk flow velocities of the anchoring and back-support pilots are 3 m/s (2.39 g/s) and 4.3 m/s (3.98 g/s), respectively. The burner is mounted on a vertical translation stage to vary the measurement locations in the flame. Turbulence intensity, integral length scale, and the Taylor microscale for this test condition measured at the burner exit location are 2.2 m/s, 2.1 mm, and 1.4 mm, respectively. These calculations assume Taylor's frozen turbulence hypothesis and have been reported in our previous publication where a high-resolution s-PIV measurement was performed [43].

3.2   Diagnostics

In order to quantify the shape of the pockets in multiple planes, a four-camera diagnostic setup was used. Figure 6(a) provides an overview of the configuration, which includes OH-PLIF, s-PIV, and Mie-scattering (MS). Figure 6(b) shows the locations of three fields of view (FOVs) downstream of the burner exit. The s-PIV setup is used to measure the velocity in the plane of the Nd:YAG laser and the Mie-scattering camera is used to separately measure, in two-dimensions, the flame edge using seeding particles in that same plane. The OH-PLIF measurement is performed in a UV laser plane that can be either aligned with the Nd:YAG laser or swept away at known distances. With flame edge data from the Mie-scattering in the main plane and the OH-PLIF in the swept plane, we can simultaneously identify pocket shapes in two planes.

The high-speed OH-PLIF laser system consists of a 532 nm Nd:YAG pump laser (Edgewave) and a dye laser (Sirah Credo). The maximum pulse energy from the dye laser at 10 kHz repetition-rate is 0.3 mJ/pulse. A periscope and a set of three cylindrical lenses are used to obtain a collimated sheet with an approximate height of 21 mm. A CMOS sensor camera (Photron FASTCAM SA1.1), coupled with an external intensifier (LaVision HS-IRO) and a 100 mm f/2.8 UV lens (Cerco) is used with a high-transmissivity interference filter (LaVision 1108760 VZ) to collect the signal at 320 nm. The field of view achieved through this setup is 50 mm x 100 mm.

For conducting s-PIV measurements, a 10 kHz dual cavity, Nd:YAG laser (Quantronix Hawk Duo) operating at 532 nm is used in forward scatter mode. A set of collimating optics are used to create a laser sheet with a sheet height of 50 mm. A pair of CMOS cameras (Photron FASTCAM SA5) equipped with 100 mm f/2.8 lenses (Tokina Macro) are used. The angle between the laser plane and each camera sensor is 25-30 degrees; the field of view obtained through this setup is 50 mm x 68 mm. Aluminum oxide particles of sizes 0.5-2 micron are used to seed the flow and 532 nm laser-illuminated images are collected at 10 kHz in double frame mode with a pulse separation of 14 µs. The particle Stokes number based on a 1 µm nominal diameter of these particles is approximately 0.06, indicating that flow oscillations up to 4000 Hz can be tracked by these particles [46]. Near-infrared filters (Schneider Kreuznach IR MTD) and laser line filters (Edmund Optics TECHSPEC 532 nm CWL) are used on each camera to reduce flame luminosity. Vector calculations are performed on the image-pairs using DaVis 8.3 from LaVision. A multi-pass cross-correlation algorithm is used with window sizes ranging from 64 x 64 to 16 x 16; for each pass, a

50% overlap is used. The resulting vector spacing is 0.99 mm/vector. Post-processing of vectors is performed with a universal outlier detection scheme with a 3x median filter. The uncertainty calculation in DaVis 8.3 is used to estimate the errors in velocity calculations; the averaged uncertainties in the instantaneous velocities are ±0.24 m/s.

The experimental setup for Mie-scattering includes a high-speed camera (Photron FASTCAM SA4) equipped with a 100 mm f/2.8 lens (Carl Zeiss Makro-Planar). The resulting field of view and image resolution is 41 mm x 38 mm and 0.11 mm/pixel, respectively. Work by Pfadler and coworkers [47] have shown that using Mie-scattering to obtain the time-averaged progress variable and flame surface density (FSD) is comparable to using OH-PLIF; however, uncertainties can arise due to insufficient seeding particle densities. Comparisons are made between OH-PLIF and Mie-scattering to quantify differences due to these uncertainties in Section 3.4.

In order to perform measurements in the same plane for OH-PLIF, s-PIV, and Mie-scattering, a dichroic mirror is used to combine the laser sheets from the OH-PLIF and the s-PIV laser systems. This dichroic mirror reflects the UV laser sheet and transmits the 532 nm laser sheet. Additionally, this mirror is mounted on a horizontal translation stage allowing for changing the measurement plane for the UV laser while keeping the 532 nm laser plane constant. All simultaneous s-PIV and Mie-scattering measurements are performed in the geometric center plane of the experiment $(x, y, 0)$ and the OH-PLIF measurements are performed for six different planes with offset values of Δz = 0.5, 1.0, 1.5, 2.0, and 4.0 mm. Additionally, data is collected only in FOV III.

3.3 Image processing techniques

OH-PLIF images are corrected for laser sheet profile variations using a signal profile taken in a region of stable, homogeneous OH generated by the laminar pilot flames; the profile is the average of 1000 images. A bilateral filter is applied to the sheet-corrected images to remove speckle noise and smooth discrete intensity changes. Otsu's method [48] is used to perform thresholding to obtain a binarized image. The flame edges are obtained using the '*bwboundaries*' function in Matlab. This built-in function traces the exterior boundaries of objects in binary images, including the boundaries of holes inside these objects. The function uses a Moore-Neighbor tracing algorithm modified by Jacob's stopping criteria [49]. Flame edges obtained from this analysis are also used for flame front tracking for flame pockets.

The process for binarization and edge detection for Mie-scattering images is as follows: (i) images are Gaussian filtered for blurring sharp gradients due to noise, (ii) median filtering with a window size of 10 pixels x 10 pixels is applied to remove the effect of salt and pepper noise due to scattering from aluminum oxide particles, (iii) smoothing operation is performed using bilateral filtering, (iv) spatial gradient of the image is obtained and Otsu's method is applied for thresholding, (v) Otsu's method is applied on the smoothed image from step (iii) for obtaining additional thresholding values ($C_{T,processed}$), (vi) threshold values from the gradient image are used as placeholders for flame edge locations to find the threshold values in the smoothed image at these locations ($C_{T,grad}$), (vii) mean of the threshold values of the processed image at the locations of the gradients and threshold value from the smoothed images is obtained ($C_{T,mean}$), and (vii) the mean threshold value is used to binarize the processed image. Images of an example of this process are provided in Figure S1 of the supplementary material.

3.4   Comparisons between OH-PLIF and Mie-scattering

Calculations of flame pocket consumption rates in 2D requires tracking of flame pocket perimeters and areas from experimental measurements. Simultaneous measurements of pockets using OH-PLIF and Mie-scattering in the same plane can identify the difference in the flame surface between these two techniques. Figure 7 shows scatter plots of pocket areas and perimeters from OH-PLIF (horizontal axis) and Mie-scattering (vertical axis) in the center plane $z=0$ mm for 5700 pockets. Here, tagging corresponding pockets between OH-PLIF and Mie-scattering is achieved by overlaying pockets from both measurement techniques; pockets from Mie-scattering that intersect pockets from OH-PLIF are tagged and area and perimeter information for tagged pockets are stored and compared.

A maximum likelihood approach for linear regression is implemented to obtain linear fits for pocket areas and perimeters between OH-PLIF and Mie-scattering. The advantage of using the likelihood estimation is that it results in a precision parameter, the inverse of the variance of the fit; maximizing the log-likelihood of this parameter allows calculation of the best fit [50]. Equations for linear regression for each fit and fit variability (σ) are shown in Figure 7. This fitting exercise shows that in the $z=0$ mm plane where the OH-PLIF and Mie-scattering laser planes overlap, pockets measured from Mie-scattering are generally smaller than that from OH-PLIF, which can be attributed to the uncertainties in the edge detection procedures for particle images.

12

The pockets detected from Mie-scattering are approximately 36% smaller than those from OH-PLIF. This difference can be due to the different quantities being measured in the two techniques (qualitative density changes in Mie-scattering and OH radical concentrations in OH-PLIF). Additionally, median filtering of Mie-scattering images can result in detection of smaller flame pocket shapes.

The pocket areas and perimeters on average agree between OH-PLIF and Mie-scattering measurements; however, there are some instances where positive values exist from Mie-scattering for near zero values from OH-PLIF. This difference is a result of the salt and pepper noise due to light scattering from aluminum oxide particles. The steps taken to binarize Mie-scattering images (Section 3.3) are able to remove this effect on average, but given the small size of these pockets, it is evident that certain pockets identified from Mie-scattering are not representative of the OH-PLIF measurements. The small proportion of these events can be considered negligible for the purpose of this study.

4   Formulation

The goal of this formulation is to more accurately calculate the consumption speed of a flame pocket, although the procedure could be applied to any out-of-plane effect discussed in Section 2. Figure 8 shows a flowchart depicting the methodology implemented in this analysis. The measured consumption rate distribution is assumed to be a mixture of two distributions (distributions 1 and 2) that represent consumption rates from out-of-plane motion and true consumption rates, respectively. In order to calculate the distribution of out-of-plane consumption rates, the 3D pocket shapes are estimated from measured 2D edges. Measured out-of-plane velocities from s-PIV are used to simulate convection of reactant 3D pockets through a stationary plane and cross-sectional pocket areas and perimeters are calculated. These geometric parameters are used to calculate the apparent reactant pocket consumption rate due to through-plane pocket convection. A PDF of this apparent consumption rate is obtained and this PDF is separated from the measured consumption rate PDF to obtain a corrected PDF, allowing for estimation of the uncertainty due to pocket convection.

The use of probabilistic modeling to estimate parameters in experimental data is becoming more popular in reacting systems. The use of Bayesian inferencing for the development of turbulence model closures has yielded promising results from a number of researchers [51]. Bayesian inferencing has also been used to assimilate data from experiments and simulation, as was done by Christopher *et al*. [52], to reduce the impact of uncertainties in boundary conditions on the results of a turbulent buoyant plume simulation. Work by Daun and coworkers used Bayesian frameworks and prior distributions to reduce uncertainty in a range of different experimental measurements, including light scattering [53], laser-induced incandescence [54], and tomography [55]. Our usage of these probabilistic techniques follows in the same vein, where we develop prior distributions from theoretical considerations to estimate measurement uncertainty due to out-of-plane motion.

4.1   Analysis of experimental data

In an experiment, we capture thousands of pockets over a one-second data collection period [56]. Using the '*bwboundaries*' algorithm in Matlab, each non-connected edge corresponding to a pocket in each frame is stored as a separate object in a cell array. Closed edges identified this way are flagged and the binarized pixel values contained in the edges (0 for reactants and 1 for products) are utilized to discern reactant pockets from product pockets. Geometrical properties for these pockets, such as contour centroid, area, perimeter, etc., are also stored along with the edges.

A tracking scheme is implemented for each reactant pocket identified using this method. First, pockets detected in consecutive images are grouped together; second, for each pocket, a search is conducted in the next frame to find the pocket of interest using a nearest distance approach with a threshold convection distance based on the bulk flow velocity and the velocity fluctuations. Third, if a pocket is identified in the next frame, a pocket number is assigned to the pocket of interest and the pocket in the consecutive frame. Steps are repeated for all the pockets until all pockets are assigned a pocket number and these numbers are updated if the pocket is no longer tracked.

We calculate the consumption rate of each pocket using Equation (1) [57-60]. This consumption rate is calculated for all pockets at each time step, resulting in a distribution of consumption rates, as shown in Figure 1. As discussed in Section 2, this distribution contains negative consumption speeds, in part because the pocket moves through the plane and the area of the pocket becomes larger as an artifact of the shape of the pocket; the measured distributions

likely also include consumption rates that are artificially high due to the out-of-plane motion. We will call this artificial consumption "out-of-plane consumption," which can be negative or positive if the shape becomes smaller or larger, respectively, as it moves through the plane.

4.2   *Estimating out-of-plane consumption*

To estimate the out-of-plane consumption rate, we create a distribution of pockets of various sizes and shapes and "measure" the consumption rate using Equation (1) by pushing pockets through the plane at velocities measured from s-PIV in simulation. In order to make this simulation as representative of the real pocket process as possible, artificial flame pockets should have geometries like those in the actual flame. We assume that a flame pocket can be described as a sphere whose shape is perturbed by a series of Legendre polynomials, as has been done in previous studies of turbulent flame propagation [61-63]. This formulation involves a few assumptions:

1. Pockets are assumed to be symmetric about the plane of the OH-PLIF laser sheet in order to create symmetric out-of-plane consumption rates. In this way, it is equally likely that the out-of-plane motion creates a positive and negative consumption rate bias.

2. It is assumed that pockets are spherical in shape with perturbations representing the 3D wrinkles [64].

3. Measured consumption rates are linear combinations of true consumption rates and the out-of-plane consumption rates.

4. Flame pockets do not rotate due to any convection or propagation effects. To support this assumption, angular momentum (ω) for each reactant pocket is calculated based on a mean angular velocity obtained along the outermost radial distance from the center of the pocket. Centroidal moment of inertias (I_{xx}, I_{yy}) are calculated from the 2D pocket edges and found to be negligible (see Figure 2S in the supplementary material).

The first instance we see a flame pocket from pocket tracking is used to identify the pocket shape and pocket flame edges (x_p, y_p) from that instance are used for construction of a modeled pocket. First, radii along the parametric flame edge (*s*) and their mean are extracted using the following equation:

$$r_p = \left[\left(x_p - \overline{x_p}\right)^2 + \left(y_p - \overline{y_p}\right)^2\right] \tag{2}$$

15

$$r_{mean} = \overline{r_p}$$

In Equation (2), r_{mean} is the mean radius of the flame pocket. The objective here is to model $r_p(s)$ as a weighted sum of Legendre polynomials. Legendre polynomials are commonly used in modeling spherical harmonics; their application to flames has been used to study wrinkling of spherically expanding flames [61]. Equation (3) shows the equations describing Legendre polynomials:

$$P_n(x) = \frac{1}{2^n n!} \frac{d^n}{dx^n} (x^2 - 1)^n$$

$$P_n(x) = \left(\frac{2n-1}{n}\right) x \, P_{n-1}(x) - \left(\frac{n-1}{n}\right) P_{n-1}(x) \tag{3}$$

To determine the number and order of the Legendre polynomials, we perform a fitting procedure. Fitting Legendre polynomials to the radius perturbation (r_p) can be achieved using least-square approximation. For this study, Legendre polynomials of a maximum order (n) of 25 are used. Coefficients for each order are calculated as:

$$A_n = \left(2 - \frac{1}{n-1} A_{n-1}\right) - \left(1 - \frac{1}{n-1} A_{n-2}\right) \tag{4}$$

Orthogonal-triangular decomposition (also known as QR decomposition) is used as a least-square approximation technique to evaluate the weights of polynomials of order n for r_p as follows:

$$\mathbf{w}_n = \mathbf{R}^{-1}(\mathbf{Q}\mathbf{r}_p)$$

$$\mathbf{D} = \mathbf{Q}\mathbf{R}$$

$$\mathbf{r}_{p,fit} = \mathbf{D}\mathbf{w}_n \tag{5}$$

$$\mathbf{D} = \prod_{i=1}^{\infty} X_i A_n, \, where \, X_i \in [-1, +1]$$

Here, $r_{p,fit}$ is the result of fitting Legendre polynomials to r_p. From this fitting, a Pearson's correlation coefficient (P_{coeff}) can be calculated to check the robustness of the fitting operation as:

$$P_{coeff} = \frac{\mathbf{a}^{\mathsf{T}}\mathbf{b}}{\mathbf{a}^{\mathsf{T}}\mathbf{a} \times \mathbf{b}^{\mathsf{T}}\mathbf{b}}$$

$$a = r_p - \bar{r}_p \tag{6}$$

$$b = r_{p,fit} - \bar{r}_{p,fit}$$

Similarly, a root-mean-squared error (RMSE) metric can be obtained to further verify the validity of fitting:

$$\text{RMSE} = \left(\frac{\mathbf{Z}^{\mathsf{T}}\mathbf{Z}}{m}\right)^{1/2}$$

$$Z = r_p - r_{p,fit} \tag{7}$$

$$m = size(r_p)$$

Figure 9(a) shows example of a typical pocket edge observed from OH-PLIF images and Figure 9(b) shows the value of r_p along the flame edge. The Pearson's coefficient and the root-mean-squared error from the fitting process is shown in Figure 9(c). A value of 0.9 for the Pearson's coefficient is used to find the order of the polynomials used for fitting the pocket radii. Figure 9(d) shows the weights of the polynomial orders with the maximum order being the cut-off value found from the value of $P_{coeff} = 0.9$.

Using the mean radius, weights, and orders of the fitted Legendre polynomials, a perturbation is created as follows:

$$Y = \sum_{n=1}^{n_{max}} w_n P_n(X)$$

$$X = \cos\phi$$

$$r' = Y - \bar{Y} \tag{8}$$

$$r'_h = r' \cos\theta$$

$$r = r_{mean}(1 + r'_h)$$

In the above equation, $r_h{'}$ is a harmonic perturbation constructed from Legendre polynomials to be used in spherical coordinates and r is the mean radius with the harmonic perturbation. Figure 10 shows examples of the procedure for creating the radius with a harmonic perturbation for the pocket shown in Figure 9(a).

Converting from spherical coordinates to Cartesian coordinates, the surface of the constructed pockets are obtained as follows:

$$x = r \sin \phi \cos \theta$$
$$y = r \sin \phi \sin \theta$$
$$z = r \cos \phi$$
$$\phi = [0, \pi]; \quad \theta = [0, 2\pi]$$

(9)

Figure 11 shows a comparison between measured flame pocket edges and the constructed 3D pocket.

Next, we numerically pass these pockets through the $(x, y, 0)$ plane in order to calculate the out-of-plane consumption speeds. For every pocket, a mask is created on the instantaneous velocity field corresponding to the first instance of the pocket using the edges obtained from OH-PLIF. Velocity values inside the pocket are extracted and averaged to obtain a single value representing the bulk out-of-plane velocity of the reactant gases inside the pocket. The modeled pocket is then pushed through the plane at that spatially-averaged velocity in order to calculate the out-of-plane consumption speed. Figure 12 shows how this is achieved: (i) 3D pockets are moved through the $(x, y, 0)$ plane, (ii) for every $\Delta t = 100\,\mu s$, cross-sectional areas and perimeters are recorded, and (iii) the out-of-plane consumption rate are calculated using Equation (1); a video in the supplementary material shows this process.

Using constructed 3D pockets and measured out-of-plane velocities, a distribution of the out-of-plane consumption rate is created, as shown in Figure 13. The shape of this distribution is modeled with a Cauchy distribution, which is a continuous distribution defined by two parameters: a center location and a scale. In statistics, it is the distribution of the ratio of two independently normally distributed random variable with zero mean [65], and in this study was the distribution that best fit the data obtained from the out-of-plane calculation. The center (median) value (μ_1) and a scale (b_1) metric is estimated for the Cauchy distribution as follows:

$$\mu_1 = \begin{cases} x_{(n+1)/2}, if\ n\ is\ odd \\ \dfrac{x_{n/2} + x_{(n+1)/2}}{2}, if\ n\ is\ even \end{cases} \tag{10}$$

$$b_1 = \frac{1}{2}\ IQR(x)$$

In these equations, IQR is the inter-quartile range of the out-of-plane consumption rate observations. These parameters are used to develop a probabilistic model for deconvolution of out-of-plane consumption rate distribution from the measured consumption rate distribution.

4.3   Comparison of modeled and measured pocket distributions

In this section, we compare the area and perimeter statistics of the real and simulated pockets in different planes to verify that the constructed pockets mimic real pocket shapes. Simultaneous OH-PLIF and Mie-scattering imaging techniques are implemented in FOV III while varying the laser plane location for OH-PLIF. The laser plane location for Mie-scattering is held constant in the $(x, y, 0)$ plane and the OH-PLIF laser plane is varied away from the center plane.

Figure 14(a,b) show the relative differences between pocket areas and perimeters measured from Mie-scattering and OH-PLIF at different OH-PLIF plane locations (Δz). Here, the differences are normalized by perimeter and area from Mie-scattering since the laser plane for Mie-scattering is held in the same place (z=0 mm). The PDF distributions indicate that as the plane offset distance is increased, the pocket areas and perimeters from OH-PLIF diverge from those from Mie-scattering. An important observation from these PDFs is that for the Δz=0 mm case, the relative difference between pocket areas and perimeters peaks around -0.4; This value indicates that there is a 40% difference between pocket areas and perimeters from Mie-scattering when compared with OH-PLIF. This result is very similar to the linear regression fit (36%) in Figure 7. The results in Figure 14(a,b) show that as the plane offset value is increased, flame pocket shape changes significantly.

In order to verify that the simulated pocket construction procedure produces representative 3D pockets, several pocket slices in the z direction are used to quantify the differences in the 2D perimeters and areas of the simulated pockets. The same six offset locations from $(x, y, 0)$ plane as in the experiment are selected. Figure 14(c,d) show PDFs of pocket area and perimeter differences relative to the center plane for different plane offset values from simulated 3D pockets. These trends indicate that as the plane offset value increases, the relative differences are quite large

when compared with smaller plane offset values. The modeled pockets are assumed to be spherical in this study and this trend is expected.

It is important to note that since the 3D shapes of the measured pockets are unknown, their centroids are also unknown. Additionally, the alignment of these centroids with the Mie-scattering plane and the pockets shapes can significantly affect the trends of the PDFs in Figure 14(a,b), as was seen in the DNS pocket study in Section 2. But, given the similarity of the trends between experimental and modeling results, it can be anticipated that the centroids for some pockets from this data set are near the z=0 mm location and that due to the large number of pockets, the displacements of the measurement planes from the pocket centroids are evenly distributed about the laser plane as the flame extends far on either side of the laser plane and flame pocket formation is equally likely on all points on the flame surface as the inflow turbulence is uniform. However, due to the limitations of the current setup, this alignment cannot be validated. The comparisons in Figure 14 show that the Legendre polynomial fitting process is able to represent the observations from experimental measurements *in the aggregate*.

4.4 Correcting the measured data

The process of synthesizing the measured data with the modeled out-of-plane consumption distributions requires separating the two PDFs and can be treated as a mixture model problem [50]. The mixture model is posed as a superposition of a univariate distribution of the out-of-plane consumption rate and the true consumption rate of reactant pockets. The combination of these two distributions is the consumption rate distribution from OH-PLIF measurements. The true consumption rate distribution is assumed to have an Inverse Gaussian distribution based on the DNS analysis in Section 2 [56]. The Inverse Gaussian distribution is a continuous distribution defined by a center and a scale metric and historically describes the distribution of time for a Brownian motion reaching a positive level with a positive drift [66]; it was also chosen in this study for its good fit to the data.

The mixture-model problem requires estimation of parameters for the true consumption rate distribution. There are several methods in estimating these parameters, but here we choose a Markov-chain Monte Carlo (MCMC) sampling algorithm as it is a robust method for estimating parameters of mixture models [50]. Python's PyMC3 module is used for Bayesian inference implementation of the mixture model problem using the No-U-Turn Sampler (NUTS) [67]. Since

20

this methodology relies on sampling based on priors, distribution models are assumed for the parameters in the mixture model and samples are drawn from these distributions to obtain likelihood functions that represent the mixture model. In the next section, development of a probabilistic model to represent the measured consumption rate distribution to be used with MCMC sampling algorithms is presented.

4.4.1 Probabilistic Model

For each distribution, a center location variable, or mean, and a metric representing the level of variance is used. For a Cauchy distribution, a center (μ_1) and a scale metric (b_1) are used, as shown in Equation (10). For an Inverse Gaussian distribution, a center (μ_2) and a scale metric (λ_2) are defined. Mixture models also rely on a mixing value; for a mixture model with two components, it can be defined for one distribution as $\hat{\pi}$ and for the other as 1-$\hat{\pi}$. Equation (11) summarizes these parameters for the model:

$$
\begin{aligned}
\mu &= [\mu_1, \mu_2] \\
b &= b_1 \\
\lambda &= \lambda_2 \\
w &= [1 - \hat{\pi}, \hat{\pi}]
\end{aligned}
\tag{11}
$$

Based on the estimation of the out-of-plane consumption rate, the mean (μ_1) and the variance metric (b_1) for distribution 1 is known:

$$
\begin{aligned}
&\underline{\text{Priors}} \\
&\mu_1, b_1
\end{aligned}
\tag{12}
$$

<div align="center">

Model

$$w = [1 - \hat{\pi}, \hat{\pi}]$$

$$f_1(x|\mu_1, b_1) = \frac{1}{\pi b_1} \left(\frac{b_1^2}{(x - \mu_1)^2 + b_1^2} \right)$$

$$f_2(x|\mu_2, \lambda_2) = \left(\frac{\lambda_2}{2\pi} \right)^{1/2} x^{-3/2} \exp\left(-\frac{\lambda_2}{2\pi} \left(\frac{x - \mu_2}{\mu_2} \right)^2 \right)$$

$$p = \sum_{k=1}^{K} w_k f_k, \quad where \; K = 2$$

</div>

(13)

Since parameters are known for distribution 1, we directly use them in the MCMC model for distribution 1. The mean (μ_2) for distribution 2 (f_2) is assumed to be a Gamma distribution ($\Gamma(1, 1)$) and the scale metric (λ_2) is also assumed to be a Gamma distribution ($\Gamma(1, 1)$). The mixing proportions are drawn from a Dirichlet distribution (Dir). Gamma distributions are chosen for μ_2 and λ_2 since these parameters are assumed to be positive; a Dirichlet distribution is a commonly used distribution for mixing variables in mixture models [68].

<div align="center">

PyMC3 Model

$$w = Dir(\alpha), \quad \alpha = [0.5, 0.5]$$

$$\mu_1 = \mu_{1,o}$$

$$b_1 = b_{1,o}$$

$$f_1(x|\mu_1, b_1) = \frac{1}{\pi b_1} \left(\frac{b_1^2}{(x - \mu_1)^2 + b_1^2} \right)$$

$$\mu_2 \sim \Gamma(\alpha = 1, \beta = 1)$$

$$\lambda_2 \sim \Gamma(\alpha = 1, \beta = 1)$$

$$f_2(x|\mu_2, \lambda_2) = \left(\frac{\lambda_2}{2\pi} \right)^{1/2} x^{-3/2} \exp\left(-\frac{\lambda_2}{2x} \left(\frac{x - \mu_2}{\mu_2} \right)^2 \right)$$

$$p(x|w, \mu, \Sigma) = \sum_{k=1}^{K} w_k f_k$$

</div>

(14)

The Markov chains are run for 6000 iterations with a burn-in sample size of 1000. Markov chain sampling data are stored for each variable in the model. The results of this simulation are provided in the next section.

5   Results

5.1   Pocket statistics

Statistics from the pocket construction analysis are presented in Figure 15; Figure 15(a) shows the histogram of mean pocket radii for pockets identified from OH-PLIF measurements. It is important to note that the UV laser sheet height restricts completely tracking large-radii pockets through burnout. However, most pockets have small radii and hence we observe the full burn-out of most pockets. Additionally, the size of most of these pockets is smaller than the integral length scale and the Taylor microscale from the incoming turbulence at the burner exit. In Figure 15(b), histograms of the spatially-averaged out-of-plane velocities within reactant pockets are shown. This histogram is not symmetric about zero, indicating that some bulk out-of-plane velocity exists and can drive pockets into and out of the measurement plane. In Figure 15(c), the histogram of the maximum Legendre polynomial used for fitting r_p is presented. Using the criterion set earlier with finding n that matches a P_{coeff} of 0.9, most of these pockets are fitted with Legendre polynomials of orders $n_{max} < 7$.

5.2   Deconvolution results - model example

In order to assess the validity of the proposed method in this study, a model example is tested where synthetic spherical pockets are generated and randomly distributed about a fixed plane. Spherical pockets are used in this initial test as the flame propagation behavior is highly predictable and allows for a transparent test of the method. These pockets are given a random through-plane convection velocity and their 2D vs. 3D consumption rates are compared directly. In this example, the 3D consumption rate as a function of time is modeled as an exponential function as $S_{C,3D} = S_{C,3D0}(1 + \gamma)^{t/\Delta t}$, where γ=0.01 and Δt=0.001 s; this form is based off the results of the DNS pocket consumption rate discussed in Section 2. Initial 3D consumption rates for these pockets are randomly sampled from a gamma distribution and their initial radii are randomly sampled from a uniform distribution. The locations of the plane with respect to the pocket centers are also randomly sampled from a uniform distribution and the bulk convection velocities of the pockets are sampled from a Gaussian distribution, representative of the current data set. Figure 16 shows the probability densities of these randomly sampled quantities.

Figure 17 shows the PDFs of consumption rates of synthetically generated spherical pockets, shrinking in size while convecting through fixed planes. As noted previously in this study, the 2D

23

consumption rates show negative values due to pocket convection through fixed planes. The PDF of true 3D consumption rates through these planes is also overlaid in this figure. Following the methodology outlined in Section 4, deconvolution of the 2D consumption rates results in a Cauchy distribution and an Inverse Gaussian distribution, where the latter represents the corrected distribution of the consumption rates. It is noteworthy that a direct comparison of this deconvoluted, corrected consumption rate distribution to the true 3D consumption rate distribution shows that the most common true 3D consumption rates are captured by the Inverse Gaussian distribution and the bias from convection resulting in negative consumption rates is removed. However, the tail of the consumption rates are over-predicted using the current approach.

5.3   Deconvolution results – experimental data

Figure 18 shows the probability densities of w, μ_2, and λ_2 from the MCMC simulations; figures in each row show the probability densities from four example Markov chains for w, μ_2, and λ_2. These plots show that all Markov chain results are converged and provide roughly the same solution for these variables. Table 1 shows the median values of μ_2, λ_2, and $\hat{\pi}$. Since pocket mean radii exist across a wide range of scales, the result presented here are decomposed based on the mean radii belonging to three categories: $r_{mean} \in [0, 2]$ mm, $r_{mean} \in [2, 4]$ mm, and $r_{mean} >$ 4 mm. Results for these different ranges show that the mean of the true distributions ranges from 0.92 - 1.13 and the scale metric ranges from 2 - 3.91. The mixing value of the mixture models ranges from 0.9 - 0.94, indicating that the true distributions are largely made up of points from the measured distributions. This is expected because a relatively small percentage of consumption rates are negative in the measured distribution. These results show that reactant gases in smaller pockets are more likely to be consumed at a rate of 1.13 m/s, whereas, larger pocket reactant gases are more likely to be consumed at a rate of 0.92 m/s. These differences may be due to flame curvature effects, although more data sets would be needed to confirm this result.

Table 1: Deconvolution PDF results

Case	μ_2	λ_2	$\hat{\pi}$
All pockets	1.11	3.18	0.91
0 mm $< r_{mean} \leq 2$ mm	1.13	3.91	0.9
2 mm $r_{mean} \leq 4$ mm	1.13	2.53	0.92
$r_{mean} >$ 4mm	0.92	2	0.94

Figure 19 shows the log-likelihood probabilities of measured consumption rates belonging to distribution 2 (left column), with the scatter plot showing the measured data set and the color corresponding to the likelihood of the data point being in the deconvoluted distribution 2. These log-likelihoods,

$$\mathcal{L}_i = \log\left(w_k f_k(x_i)\right) \tag{15}$$

are dependent on the weights of each distribution and the distribution shape. A comparison of the shapes of distributions 1 and 2 shows that probabilities of consumption rates near zero are higher for distribution 1, when compared with distribution 2. For each observed sample, the log-likelihood values can be compared to categorize the sample to belong to either distribution 1 or 2:

$$z_i = \arg\max(\mathcal{L}) \tag{16}$$

Using Equation (16), it can be seen that a majority of the observed samples (as high as 91-95 %) have the likelihood of belonging to distribution 2, indicating that using the current approach, the estimated percentage of out-of-plane consumption rates to be found in the measured consumption rates is relatively low (Figure 19). The interpretation of this result is that out-of-plane effects for pocket consumption rates are low in the current experimental measurements using the current model. Further comparison of the measured and true PDFs is shown in Figure 20, confirming these results and showing the final output of this methodology, which is a "true" PDF of pocket consumption rates.

6   Conclusions

In this work, a framework is presented to use probabilistic modeling for parametric estimation to better understand the out-of-plane effects that arise in 2D measurements of 3D flame propagation. While the technique implemented for this framework relies on some assumptions about turbulent flame pockets, it provides a methodology to estimate the effect of the flame surface convection into the measurement plane by utilizing flame structure and velocity field measurements. One of the unique features of this method is that it constructs model statistics (out-of-plane consumption rates) using detailed information from the measurement itself (pocket radii and through-plane velocities), rather than generalizations about the structure and dynamics of turbulent flames. The advantage of this methodology is that it creates statistics that are uniquely

dependent on each data set and relies on relatively inexpensive computational efforts to "model" pocket motions. This framework is particularly attractive as compared to DNS, which we have shown in Section 2 is too computationally expensive to use for generating large-number statistics. Even if an experiment could be accurately simulated in DNS, the computational expense required to capture a large number of pockets is intractable. It is noteworthy here, however, that the accuracy of the results from this methodology will be dependent on the distribution model selection for deconvolution. As such, proper validation techniques will be necessary for estimation of statistically significant results.

This methodology could be extended to other sources of bias that occur in the 2D measurement of 3D flame surfaces. As discussed in Section 2, other sources of error in the 2D consumption rate calculation include orientation and location of flame pockets with respect to the measurement plane, high aspect ratio pocket shapes, the non-convex nature of the flame surface, and the highly dynamic events such as flame pinch-off. These errors could be corrected for in a similar manner as is presented here. For example, the orientation of measurement plane and the complex pocket shape effects can be easily modeled using 3D pocket shapes and in-plane pocket motions measured from experiments. In future, each of these errors could be modeled using the methodology outlined in Section 4.2 and then a multi-component mixture model could be solved using MCMC, allowing for estimation of the magnitude of each of the 2D measurement errors. These developments will be tested on both simulation as well as experimental data in order to better understand the biases that arise from the use of experimental data. The use of flame surfaces from DNS or level-set modeling will be important validation for these tools, particularly at higher turbulence intensities or in more complicated flame shapes like swirl-stabilized flames where out-of-plane motion is significant. By basing the error estimation distributions in rigorous theory and large statistics, we can have confidence in both the source of the correction as well as its statistical significance.

7 Acknowledgements

8   References

[1] A.W. Skiba, T.M. Wabel, C.D. Carter, S.D. Hammack, J.E. Temme, T. Lee, J.F. Driscoll, Reaction layer visualization: A comparison of two PLIF techniques and advantages of kHz-imaging, Proceedings of the Combustion Institute 36 (2017) 4593-4601.

[2] S.A. Filatyev, J.F. Driscoll, C.D. Carter, J.M. Donbar, Measured properties of turbulent premixed flames for model assessment, including burning velocities, stretch rates, and surface densities, Combustion and Flame 141 (2005) 1-21.

[3] J.R. Osborne, S.A. Ramji, C.D. Carter, S. Peltier, S. Hammack, T. Lee, A.M. Steinberg, Simultaneous 10 kHz TPIV, OH PLIF, and CH 2 O PLIF measurements of turbulent flame structure and dynamics, Experiments in Fluids 57 (2016) 65.

[4] R.K. Cheng, B. Bédat, L.W. Kostiuk, Effects of buoyancy on lean premixed V-flames Part I: laminar and turbulent flame structures, Combustion and Flame 116 (1999) 360-375.

[5] T. Sponfeldner, I. Boxx, F. Beyrau, Y. Hardalupas, W. Meier, A.M. Taylor, On the alignment of fluid-dynamic principal strain-rates with the 3D flamelet-normal in a premixed turbulent V-flame, Proceedings of the Combustion Institute 35 (2015) 1269-1276.

[6] N.A. Worth, J.R. Dawson, Cinematographic OH-PLIF measurements of two interacting turbulent premixed flames with and without acoustic forcing, Combustion and Flame 159 (2012) 1109-1126.

[7] I. Boxx, M. Stöhr, C. Carter, W. Meier, Temporally resolved planar measurements of transient phenomena in a partially pre-mixed swirl flame in a gas turbine model combustor, Combustion and Flame 157 (2010) 1510-1525.

[8] S.K. Thumuluru, T. Lieuwen, Characterization of acoustically forced swirl flame dynamics, Proceedings of the Combustion Institute 32 (2009) 2893-2900.

[9] P. Petersson, J. Olofsson, C. Brackman, H. Seyfried, J. Zetterberg, M. Richter, M. Aldén, M.A. Linne, R.K. Cheng, A. Nauert, Simultaneous PIV/OH-PLIF, Rayleigh thermometry/OH-PLIF and stereo PIV measurements in a low-swirl flame, Applied optics 46 (2007) 3928-3936.

[10] I. Boxx, C. Heeger, R. Gordon, B. Böhm, A. Dreizler, W. Meier, On the importance of temporal context in interpretation of flame discontinuities, Combustion and Flame 156 (2009) 269.

[11] J. Nygren, J. Hult, M. Richter, M. Aldén, M. Christensen, A. Hultqvist, B. Johansson, Three-dimensional laser induced fluorescence of fuel distributions in an HCCI engine, Proceedings of the Combustion Institute 29 (2002) 679-685.

[12] R. Wellander, M. Richter, M. Aldén, Time resolved, 3D imaging (4D) of two phase flow at a repetition rate of 1 kHz, Optics express 19 (2011) 21508-21514.

[13] T. Li, J. Pareja, L. Becker, W. Heddrich, A. Dreizler, B. Böhm, Quasi-4D laser diagnostics using an acousto-optic deflector scanning system, Applied Physics B 123 (2017) 78.

[14] I.G. Boxx, C.D. Carter, W. Meier. Investigation of turbulent lifted planar jet flames using highspeed laser imaging diagnostics. In 52nd Aerospace Sciences Meeting; 2014. p. 0316.

[15] Y. Gong, Q. Guo, J. Zhang, P. Fan, Q. Liang, G. Yu, Impinging flame characteristics in an opposed multiburner gasifier, Industrial & Engineering Chemistry Research 52 (2013) 3007-3018.

[16] E. Kristensson, Z. Li, E. Berrocal, M. Richter, M. Aldén, Instantaneous 3D imaging of flame species using coded laser illumination, Proceedings of the Combustion Institute 36 (2017) 4585-4591.

[17] M.L. Greene, V. Sick, Volume-resolved flame chemiluminescence and laser-induced fluorescence imaging, Applied physics b 113 (2013) 87-92.

[18] L. Ma, Q. Lei, J. Ikeda, W. Xu, Y. Wu, C.D. Carter, Single-shot 3D flame diagnostic based on volumetric laser induced fluorescence (VLIF), Proceedings of the Combustion Institute 36 (2017) 4575-4583.

[19] B.R. Halls, P. Hsu, S. Roy, T. Meyer, J. Gord, Two-color volumetric laser-induced fluorescence for 3D OH and temperature fields in turbulent reacting flows, Optics letters 43 (2018) 2961-2964.

[20] T. Li, J. Pareja, F. Fuest, M. Schütte, Y. Zhou, A. Dreizler, B. Böhm, Tomographic imaging of OH laser-induced fluorescence in laminar and turbulent jet flames, Measurement Science and Technology 29 (2017) 015206.

[21] B.R. Halls, N. Jiang, T.R. Meyer, S. Roy, M.N. Slipchenko, J.R. Gord, 4D spatiotemporal evolution of combustion intermediates in turbulent flames using burst-mode volumetric laser-induced fluorescence, Optics letters 42 (2017) 2830-2833.

[22] Y. Wu, W. Xu, Q. Lei, L. Ma, Single-shot volumetric laser induced fluorescence (VLIF) measurements in turbulent flows seeded with iodine, Optics express 23 (2015) 33408-33418.

[23] L. Ma, Q. Lei, T. Capil, S.D. Hammack, C.D. Carter, Direct comparison of two-dimensional and three-dimensional laser-induced fluorescence measurements on highly turbulent flames, Optics Letters 42 (2017) 267-270.

[24] B. Coriton, J.H. Frank, Impact of heat release on strain rate field in turbulent premixed Bunsen flames, Proceedings of the Combustion Institute 36 (2017) 1885-1892.

[25] B. Coriton, J.H. Frank, High-speed tomographic PIV measurements of strain rate intermittency and clustering in turbulent partially-premixed jet flames, Proceedings of the Combustion Institute 35 (2015) 1243-1250.

[26] B. Coriton, A.M. Steinberg, J.H. Frank, High-speed tomographic PIV and OH PLIF measurements in turbulent reactive flows, Experiments in fluids 55 (2014) 1743.

[27] P. Trunk, I. Boxx, C. Heeger, W. Meier, B. Böhm, A. Dreizler, Premixed flame propagation in turbulent flow by means of stereoscopic PIV and dual-plane OH-PLIF at sustained kHz repetition rates, Proceedings of the combustion institute 34 (2013) 3565-3572.

[28] L. Piegl, On NURBS: a survey, IEEE Computer Graphics and Applications 11 (1991) 55-71.

[29] B. Peterson, E. Baum, B. Böhm, A. Dreizler, Early flame propagation in a spark-ignition engine measured with quasi 4D-diagnostics, Proceedings of the Combustion Institute 35 (2015) 3829-3837.

[30] S.W. Grib, Laminar and Turbulent Study of Combustion in Stratified Environments Using Laser Based Measurements, (2018).

[31] J.B. Bell, M.S. Day, J.F. Grcar, M.J. Lijewski, J.F. Driscoll, S.A. Filatyev, Numerical simulation of a laboratory-scale turbulent slot flame, Proceedings of the combustion institute 31 (2007) 1299-1307.

[32] D. Dasgupta, W. Sun, M. Day, T. Lieuwen, Effect of turbulence–chemistry interactions on chemical pathways for turbulent hydrogen–air premixed flames, Combustion and Flame 176 (2017) 191-201.

[33] A. Amato, M. Day, R.K. Cheng, J. Bell, D. Dasgupta, T. Lieuwen, Topology and burning rates of turbulent, lean, H2/air flames, Combustion and Flame 162 (2015) 4553-4565.

[34] L. Ma, Y. Wu, Q. Lei, W. Xu, C.D. Carter, 3D flame topography and curvature measurements at 5 kHz on a premixed turbulent Bunsen flame, Combustion and Flame 166 (2016) 66-75.

[35] W. Cai, X. Li, L. Ma, Practical aspects of implementing three-dimensional tomography inversion for volumetric flame imaging, Applied optics 52 (2013) 8106-8116.

[36] A. Marshall, J. Lundrigan, P. Venkateswaran, J. Seitzman, T. Lieuwen, Fuel effects on leading point curvature statistics of high hydrogen content fuels, Proceedings of the Combustion Institute 35 (2015) 1417-1424.

[37] A. Marshall, J. Lundrigan, P. Venkateswaran, J. Seitzman, T. Lieuwen, Measurements of Stretch Statistics at Flame Leading Points for High Hydrogen Content Fuels, Journal of Engineering for Gas Turbines and Power 139 (2017) 111503.

[38] C. Chan, K. Lau, W. Chin, R. Cheng. Freely propagating open premixed turbulent flames stabilized by swirl. In Symposium (International) on Combustion; 1992: Elsevier. p. 511-518.

[39] R. Cheng, Velocity and scalar characteristics of premixed turbulent flames stabilized by weak swirl, Combustion and flame 101 (1995) 1-14.

[40] M. Zhang, J. Wang, W. Jin, Z. Huang, H. Kobayashi, L. Ma, Estimation of 3D flame surface density and global fuel consumption rate from 2D PLIF images of turbulent premixed flame, Combustion and Flame 162 (2015) 2087-2097.

[41] L. Ma, Y. Wu, W. Xu, S.D. Hammack, T. Lee, C.D. Carter, Comparison of 2D and 3D flame topography measured by planar laser-induced fluorescence and tomographic chemiluminescence, Applied Optics 55 (2016) 5310-5315.

[42] A. Tyagi, I. Boxx, S. Peluso, J. O'Connor, Pocket formation and behavior in turbulent premixed flames, Combustion and Flame 211 (2020) 312-324.

[43] A. Tyagi, I. Boxx, S. Peluso, J. O'Connor, Statistics and topology of local flame–flame interactions in turbulent flames, Combustion and Flame 203 (2019) 92-104.

[44] P.E. Hamlington, R. Darragh, C.A. Briner, C.A. Towery, B.D. Taylor, A.Y. Poludnenko, Lagrangian analysis of high-speed turbulent premixed reacting flows: Thermochemical trajectories in hydrogen–air flames, Combustion and Flame 186 (2017) 193-207.

[45] S.H. Preetham, T.C. Lieuwen, Response of turbulent premixed flames to harmonic acoustic forcing, Proceedings of the Combustion Institute 31 (2007) 1427-1434.

[46] F. Picano, F. Battista, G. Troiani, C.M. Casciola, Dynamics of PIV seeding particles in turbulent premixed flames, Experiments in Fluids 50 (2011) 75-88.

[47] S. Pfadler, F. Beyrau, A. Leipertz, Flame front detection and characterization using conditioned particle image velocimetry (CPIV), Optics Express 15 (2007) 15444-15456.

[48] R.C. Gonzalez, R.E. Woods, Digital image processing, Prentice Hall, Upper Saddle River, NJ, (2002).

[49] R.C. Gonzalez, R. E. Woods, and S. L. Eddins, Digital image processing using Matlab. 2004, New Jersey, Pearson Prentice Hall.

[50] C.M. Bishop, Pattern recognition and machine learning, Springer2006.

[51] K. Duraisamy, G. Iaccarino, H. Xiao, Turbulence modeling in the age of data, Annual Review of Fluid Mechanics 51 (2019) 357-377.

[52] J.D. Christopher, N.T. Wimer, C. Lapointe, T.R. Hayden, I. Grooms, G.B. Rieker, P.E. Hamlington, Parameter estimation for complex thermal-fluid flows using approximate Bayesian computation, Physical Review Fluids 3 (2018) 104602.

[53] D. Burr, K. Daun, O. Link, K. Thomson, G. Smallwood, Determination of the soot aggregate size distribution from elastic light scattering through Bayesian inference, Journal of Quantitative Spectroscopy and Radiative Transfer 112 (2011) 1099-1107.

[54] P.J. Hadwin, T. Sipkens, K. Thomson, F. Liu, K. Daun, Quantifying uncertainty in soot volume fraction estimates using Bayesian inference of auto-correlated laser-induced incandescence measurements, Applied Physics B 122 (2016) 1.

[55] K.J. Daun, S.J. Grauer, P.J. Hadwin, Chemical species tomography of turbulent flows: discrete ill-posed and rank deficient problems and the use of prior information, Journal of Quantitative Spectroscopy and Radiative Transfer 172 (2016) 58-74.

[56] A.F. Ibarreta, J.F. Driscoll, Measured burning velocities of stretched inwardly propagating premixed flames, Proceedings of the Combustion Institute 28 (2000) 1783-1791.

[57] F. Baillot, A. Bourehla, Burning velocity of pockets from a vibrating flame experiment, Combustion Science and Technology 126 (1997) 201-224.

[58] A. Johchi, Y. Naka, M. Shimura, M. Tanahashi, T. Miyauchi, Investigation on rapid consumption of fine scale unburned mixture islands in turbulent flame via 10 kHz simultaneous CH–OH PLIF and SPIV, Proceedings of the Combustion Institute 35 (2015) 3663-3671.

[59] M. Shimura, A. Johchi, M. Tanahashi, Consumption rate characteristics of a fine-scale unburnt mixture in a turbulent jet premixed flame by high repetition rate PLIF and SPIV, Journal of Thermal Science and Technology 11 (2016) JTST0047-JTST0047.

[60] R. Addabbo, J. Bechtold, M. Matalon, Wrinkling of spherically expanding flames, Proceedings of the Combustion Institute 29 (2002) 1527-1535.

[61] J. Bechtold, M. Matalon, Hydrodynamic and diffusion effects on the stability of spherically expanding flames, Combustion and Flame 67 (1987) 77-90.

[62] M. Matalon, On flame stretch, Combustion Science and Technology 31 (1983) 169-181.

[63] C. Sun, C. Law. On the consumption of fuel pockets via inwardly propagating flames. In Symposium (International) on Combustion; 1998: Elsevier. p. 963-970.

[64] S. Kotz, N. Balakrishnan, N.L. Johnson, Continuous multivariate distributions, Volume 1: Models and applications, John Wiley & Sons2004.

[65] R. Chhikara, The Inverse Gaussian Distribution: Theory: Methodology, and Applications, CRC Press1988.

[66] M.D. Hoffman, A. Gelman, The No-U-Turn sampler: adaptively setting path lengths in Hamiltonian Monte Carlo, Journal of Machine Learning Research 15 (2014) 1593-1623.

[68] D. Görür, C.E. Rasmussen, Dirichlet process gaussian mixture models: Choice of the base distribution, Journal of Computer Science and Technology 25 (2010) 653-664.
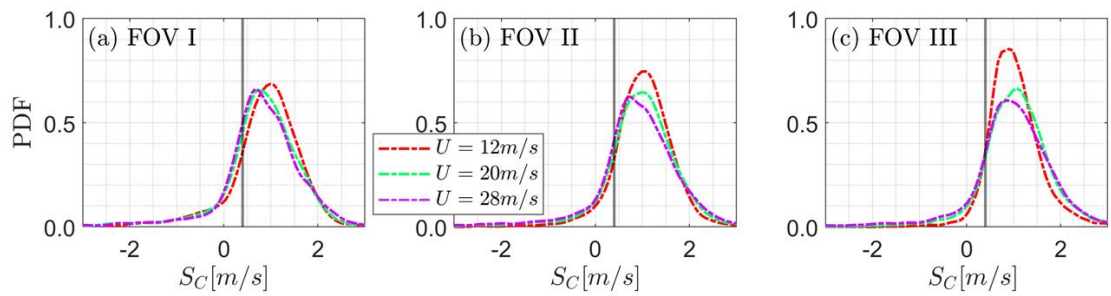
Figure 1. PDFs of reactant pocket consumption speeds in field of view (FOV) (a) I, (b) II, and (c) III for single Bunsen flames. Vertical lines represent s_L=0.4 m/s
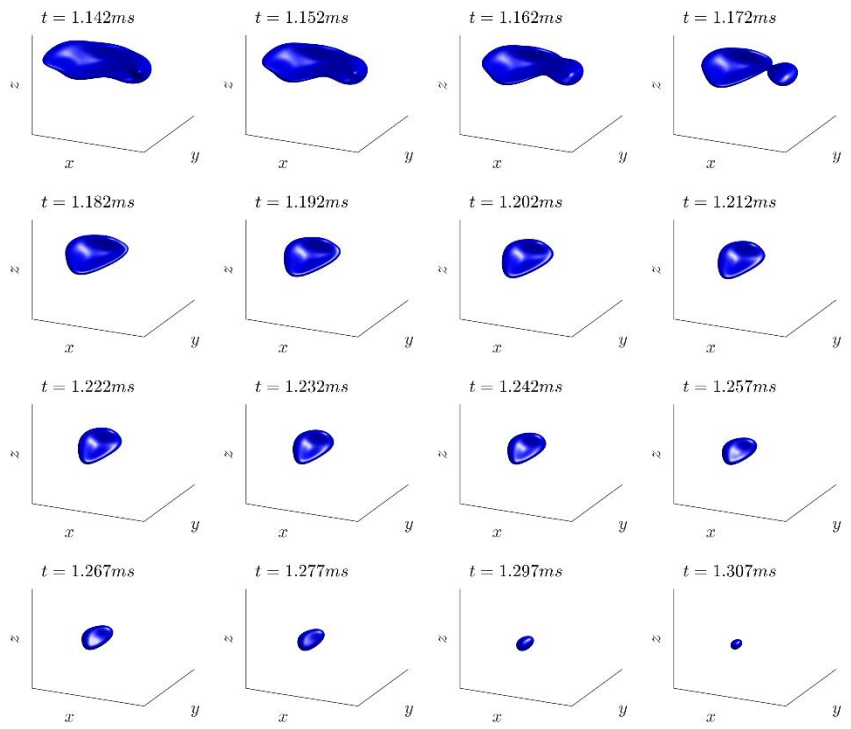
Figure 2. Time-series of 3D pocket; video provided in supplementary material. The pockets here correspond to the 1800 K temperature isosurfaces
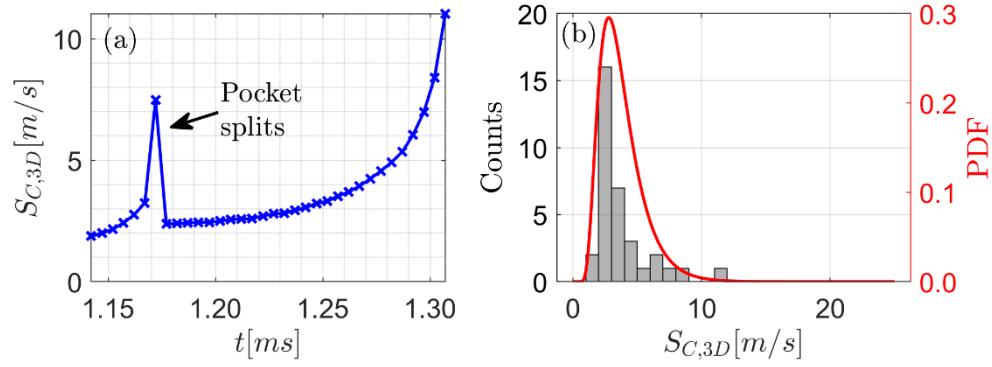
Figure 3. (a) DNS pocket consumption rate through time and (b) histogram of consumption rates
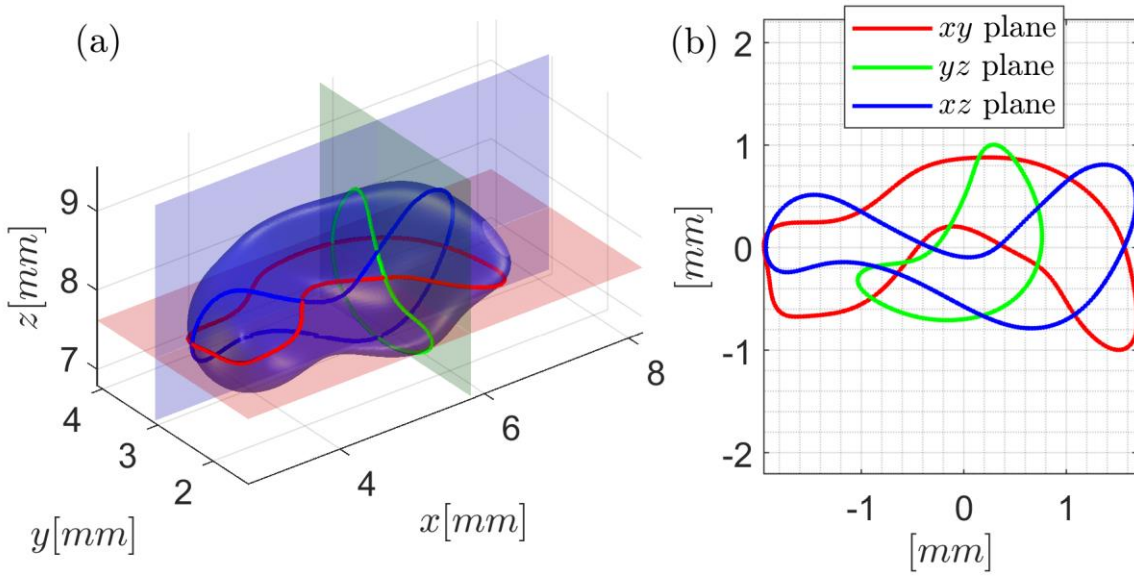
Figure 4. (a) Flame pocket shape in 3D and (b) planar cuts of the pocket along the xy, yz, and xz planes at the centroid location of the pocket
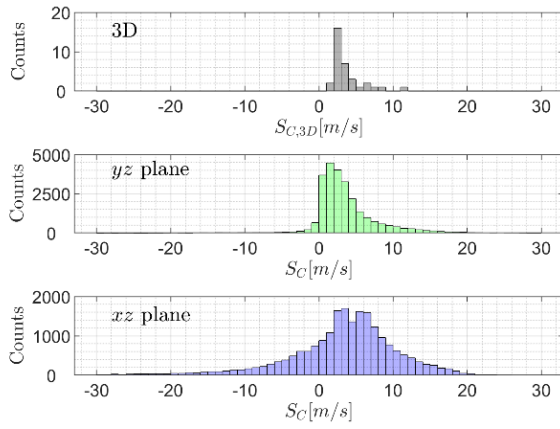
(a)
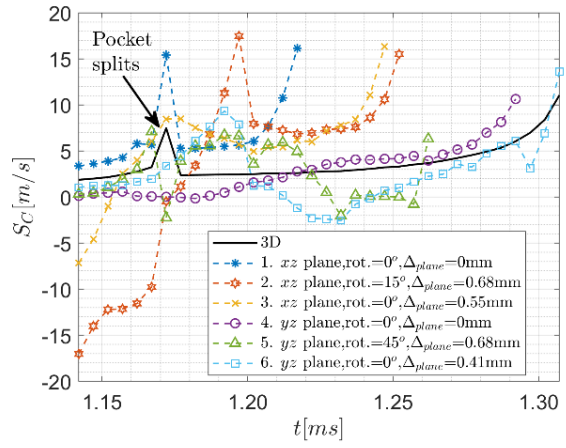
(b)

Figure 5. 2D pocket consumption rate (a) histograms and (b) time series.
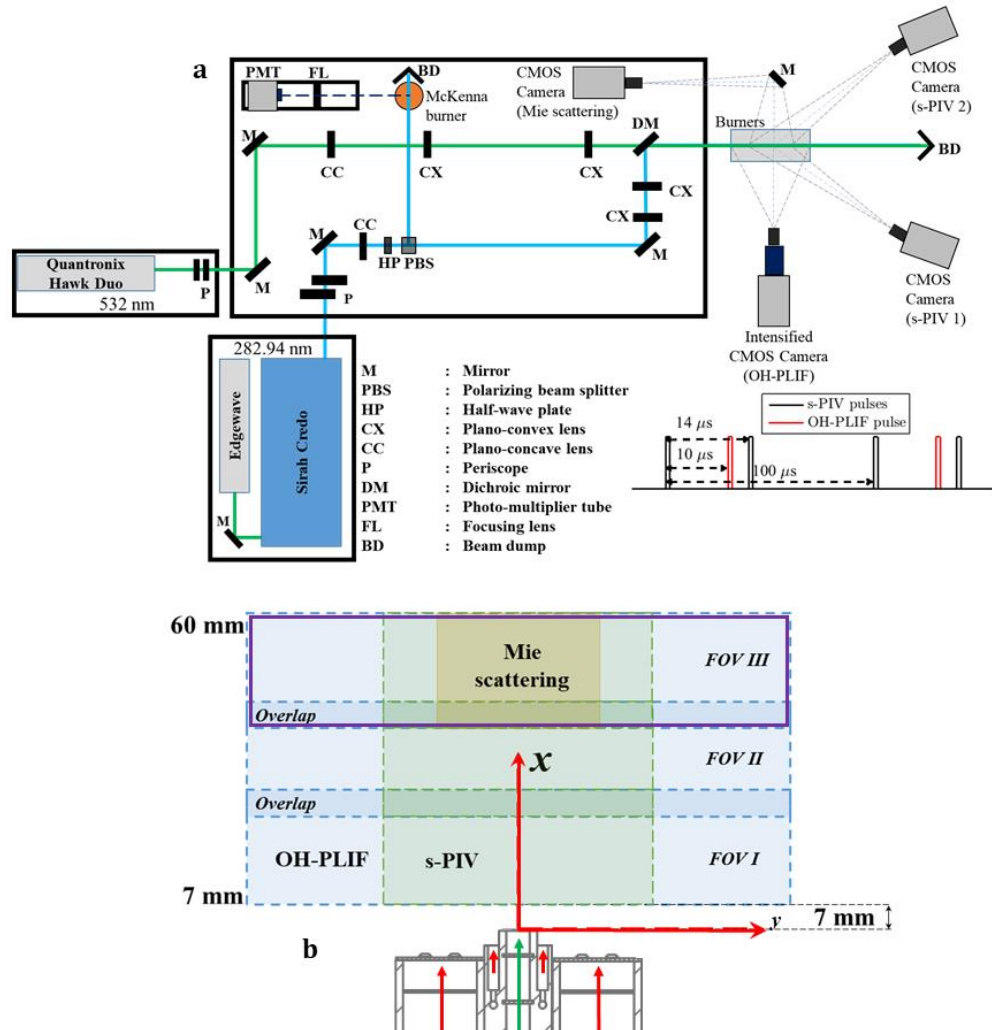
Figure 6. (a) Laser optical setup and (b) measurement locations with respect to the burner exit location. In sub-figure (b), the red arrows correspond to the flow for the back-support and anchoring pilot flames and the green arrow corresponds to the flow for the main flame
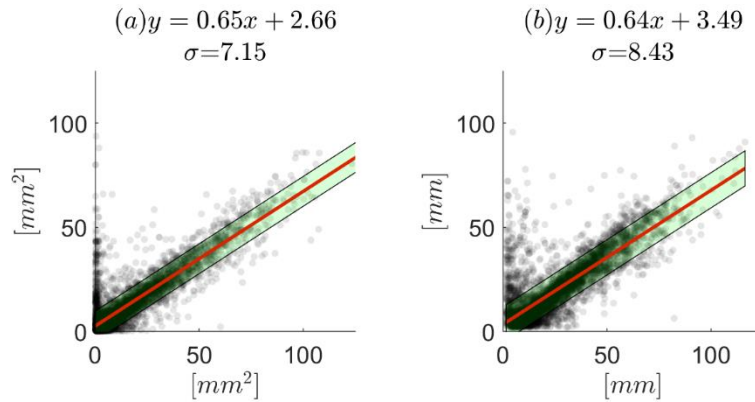
Figure 7. Scatter plots of flame pocket areas and perimeters from OH-PLIF and Mie-scattering measurements for *z*=0 mm plane. Left sub-figure compares the pocket areas and sub-right figure compares the pocket perimeters. In each sub-figure, the horizontal axis is the data from OH-PLIF and the vertical axis is the data from Mie-scattering. Green shaded regions represent the extent of *σ* for the linear fit line shown in red
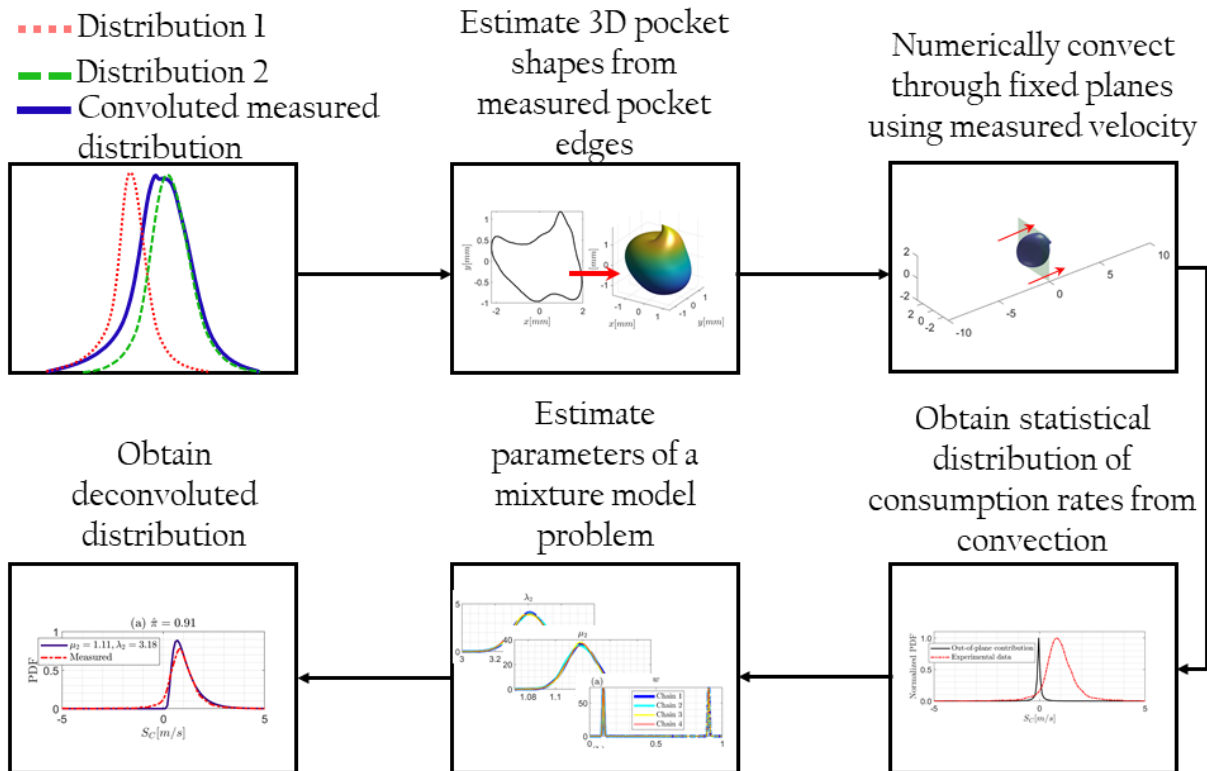
Figure 8. Flowchart of the framework for obtaining true consumption rates from measured consumption rates
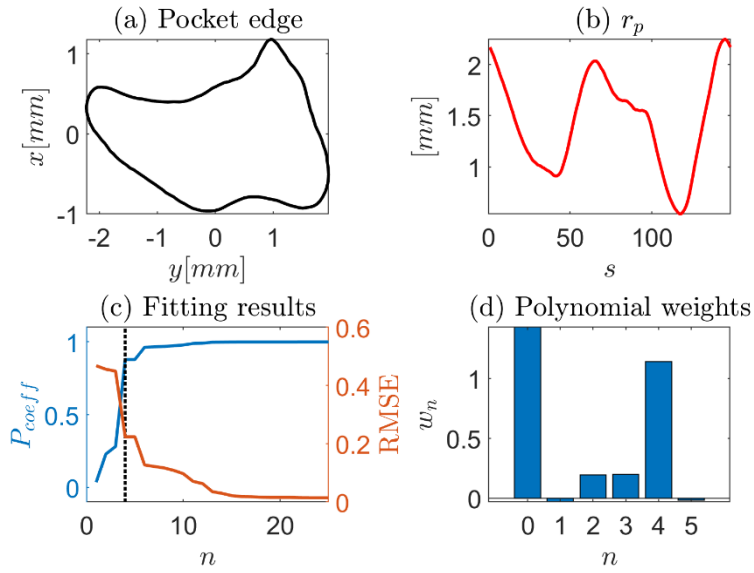
Figure 9. (a) Centered flame edge, (b) value of r_p along flame edge, (c) P_{coeff} and RMSE, and (d) w_n for fitting with a maximum polynomial order of 7
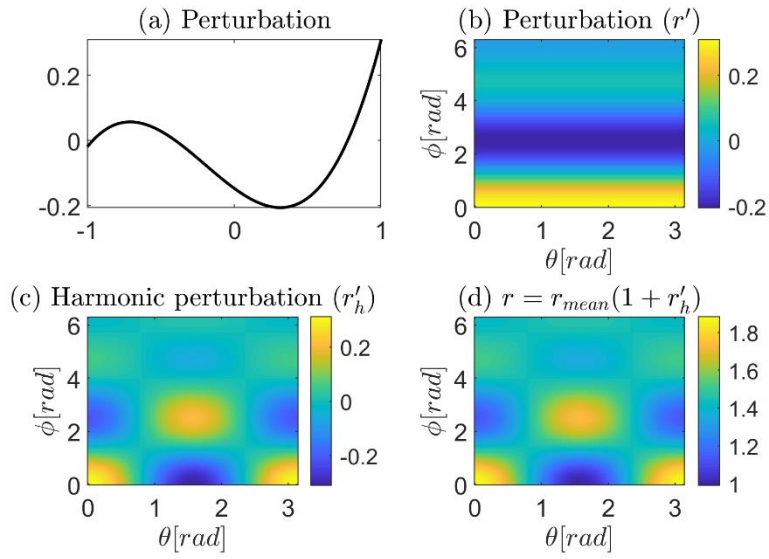
Figure 10. (a) Weighted sum of Legendre polynomials over [-1, +1], (b) perturbation radius, (c) harmonic perturbation radius, and (d) mean radius with harmonic perturbation
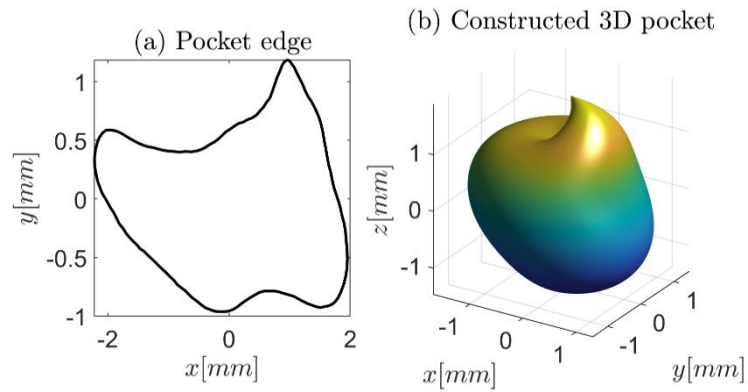
Figure 11. (a) Flame pocket edge and (b) constructed 3D pocket
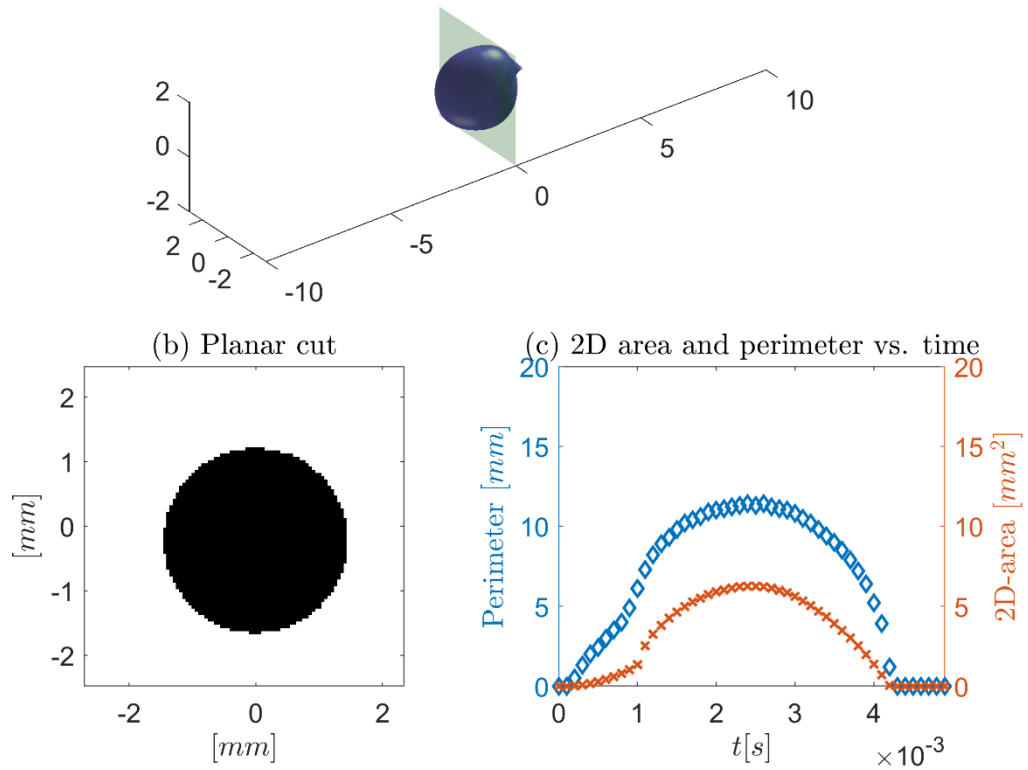
Figure 12. (a) Convection of 3D pocket through $(x, y, 0)$ plane, (b) cross-section pocket contour, and (c) time-series of cross-section area and perimeter; video provided in supplementary material.
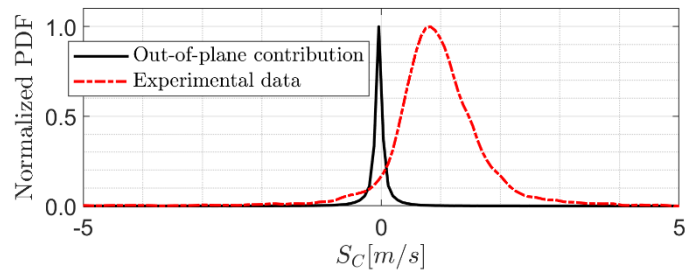
Figure 13. Out-of-plane consumption rate PDF for 3D pockets (solid black line).
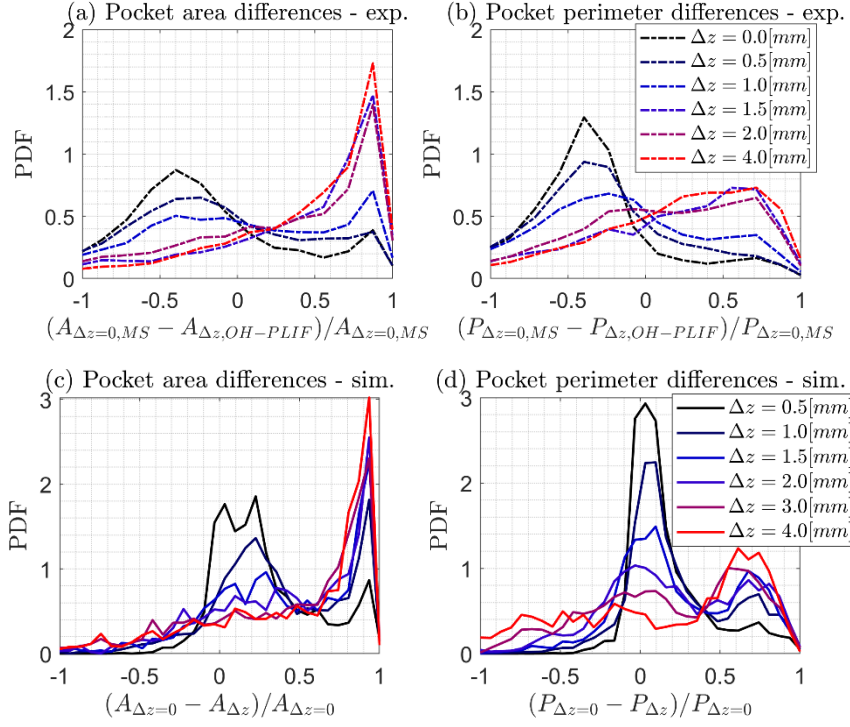
Figure 14. Relative differences in experimentally measured pocket (a) areas and (b) perimeters for different plane offset values. Relative differences in constructed 3D pockets: (c) areas and (d) perimeters for different slices
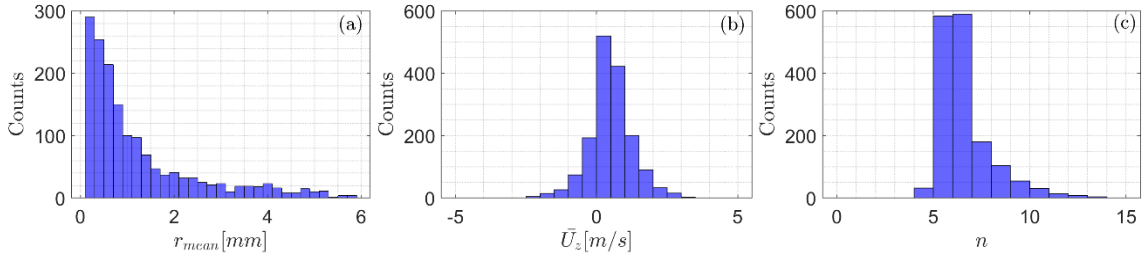
Figure 15. Histograms of (a) mean pocket radii (r_{mean}), (b) mean out-of-plane velocities inside pockets, and (c) maximum value of n_{max} used.
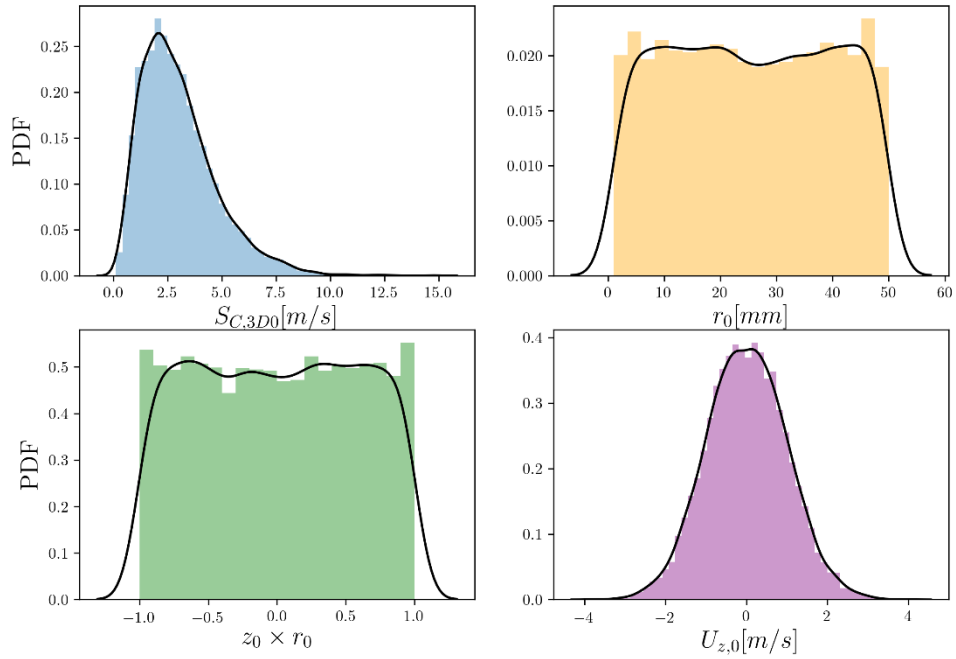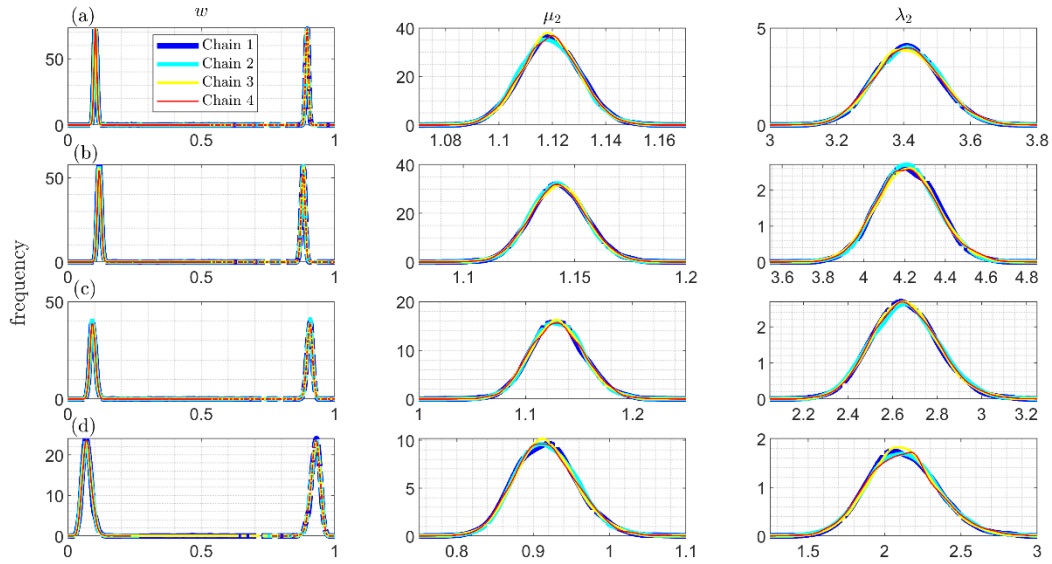
Figure 16. Probability densities of (a) $S_{C,3D0}$, (b) r_0, (c) $z_0 \times r_0$, and (d) $U_{z,0}$
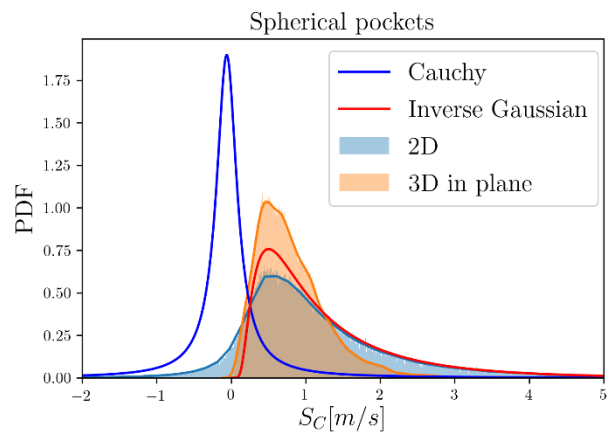
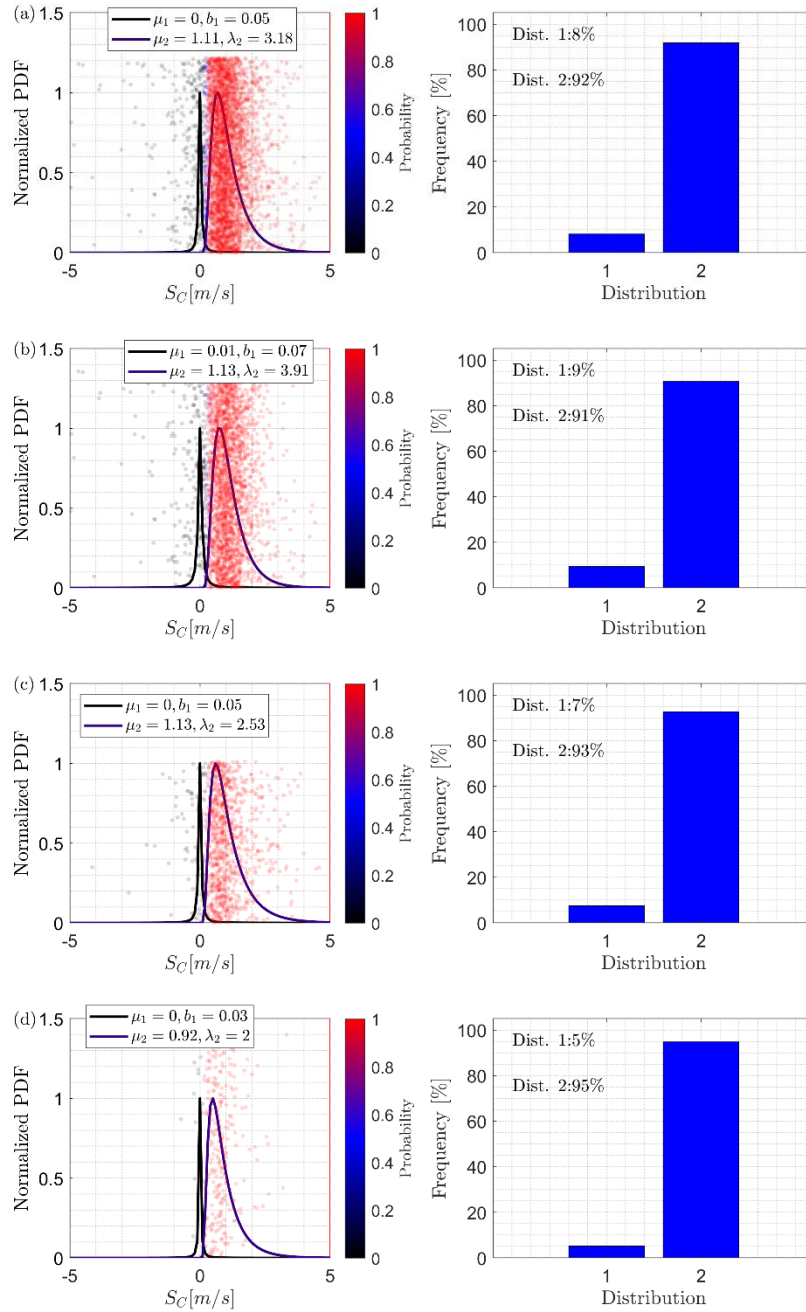
Figure 17. Deconvolution results for spherical pockets

Figure 18. Probability densities of Markov chains for variables in the model: w, μ_2, λ_2 for (a) all pockets, (b) pockets with 0 mm < $r_{mean} \leq$ 2 mm, (c) pockets with 2 mm < $r_{mean} \leq$ 4 mm, (d) pockets with r_{mean} > 4mm

Figure 19. Deconvolution of out-of-plane consumption rate PDFs from measured PDFs for (a) all pockets, (b) pockets with 0 mm < $r_{mean} \leq$ 2 mm, (c) pockets with 2 mm < $r_{mean} \leq$ 4 mm, (d) pockets with r_{mean}> 4mm
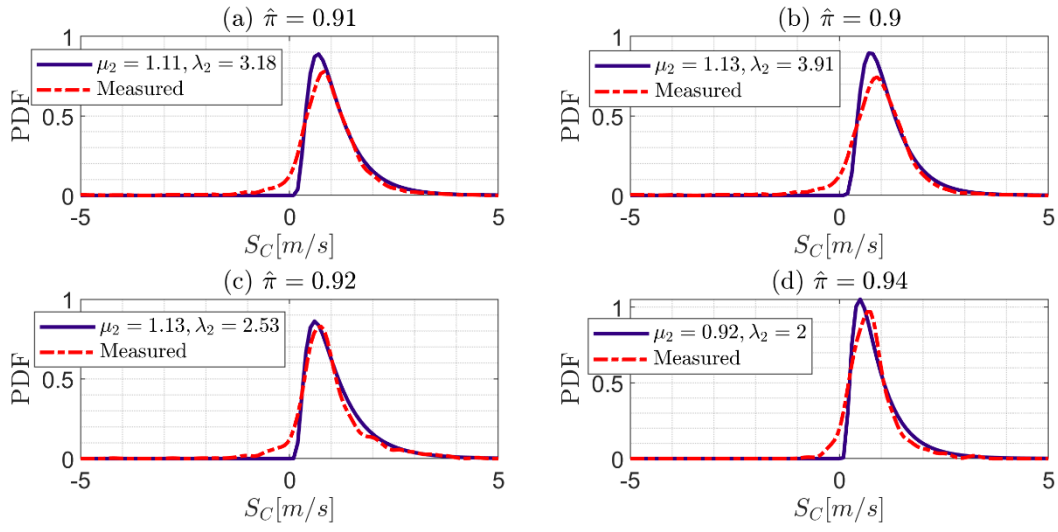
Figure 20. Comparisons between deconvoluted and measured PDFs for (a) all pockets, (b) pockets with 0 mm < r_{mean} ≤ 2 mm, (c) pockets with 2 mm < r_{mean} ≤ 4 mm, (d) pockets with r_{mean} > 4mm